CRACK DEPTH MEASUREMENT IN REINFORCED CONCRETE USING ULTRASONIC TECHNIQUES

A Thesis
Presented to
The Academic Faculty

by

Kevin C. Arne

In Partial Fulfillment
of the Requirements for the Degree
Master of Science in the
School of Civil and Environmental Engineering

Georgia Institute of Technology
May 2014

CRACK DEPTH MEASUREMENT IN REINFORCED CONCRETE USING ULTRASONIC TECHNIQUES

Approved by:

Professor Laurence J. Jacobs, Advisor
School of Civil and Environmental Engineering
Georgia Institute of Technology

Professor Kimberly Kurtis
School of Civil and Environmental Engineering
Georgia Institute of Technology

Dr. Jin-Yeon Kim
School of Civil and Environmental Engineering
Georgia Institute of Technology

Date Approved: April 7, 2014

ACKNOWLEDGEMENTS

I would like to thank Professor Laurence J. Jacobs for being a supportive advisor and a generous mentor. Talking with Professor Jacobs gave me boosts of confidence and enthusiasm as I encountered the challenges of my academic career.

Dr. Jin-Yeon Kim and Dr. Chi-Won In were both invaluable in helping me get started on my path to understanding diffuse ultrasonics. Both of them were indispensable resources I could call upon whenever I needed help, whether it was an explanation of the intricacies of the diffusion equation or just an extra set of hands in the lab.

I would also like to thank Professor Kimberly E. Kurtis for serving as a member on my committee as well as for always pointing me in the right direction on all things concrete. Professor Lawrence F. Kahn was also a great help with the design and mechanical testing setup for our concrete beams.

Many thanks go to the friends I have made and spent time with during my years at Georgia Tech. They have greatly enriched my life. Most significantly, I would like to thank my parents, family, B. G. Piper, and Charleen Wilcox for their love and support as I navigated through the good and bad of graduate life.

TABLE OF CONTENTS

ACKNOWLEDGEMENTS . . . . . **iii**

LIST OF TABLES . . . . . **vi**

LIST OF FIGURES . . . . . **vii**

SUMMARY . . . . . **ix**

I INTRODUCTION **1**

1.1 Motivation 1

1.2 Literature Review 1

1.2.1 Impact-Echo Method 1

1.2.2 Time of Flight Diffraction Method 2

1.2.3 Surface Wave Transmission Method 3

1.2.4 Diffusion Method 5

1.3 Objective 7

II THEORETICAL BACKGROUND **8**

2.1 Wave Propagation in Elastic Media 8

2.1.1 Derivation of Law of Motion 8

2.1.2 Law of Refraction 9

2.2 Time of Flight Diffraction 11

2.2.1 Background 11

2.2.2 Derivation of the depth equation 12

2.3 Diffusion Approximation 13

2.3.1 Background 13

2.3.2 Derivation of the Diffusion Equation 13

2.3.3 Solutions to the Diffusion Equation 14

III EXPERIMENTAL PROCEDURE **17**

3.1 Specimen Preparation 17

3.1.1 Specimen Design 17

3.1.2 Material Properties 20
3.1.3 Loading 20
3.2 Time of Flight Diffraction 22
3.2.1 Instrumentation 22
3.2.2 Data Processing 22
3.3 Diffusion Approximation 25
3.3.1 Instrumentation 25
3.3.2 Diffuse Data Processing 26
3.3.3 Finite Element Model 31
3.4 Crack Depth Validation 32
IV RESULTS AND DISCUSSION 35
4.1 Results 35
4.1.1 #6 Bar Beam 35
4.1.2 #8 Bar Beam 38
4.1.3 #7 Bar Beam 41
4.1.4 Summary 43
4.2 Discussion 43
V CONCLUSION AND FUTURE WORK 45
5.1 Conclusion 45
5.2 Future Work 45
REFERENCES 47

LIST OF TABLES

1 Beam Details 20

2 Compressive Strength of Concrete 20

3 Maximum Loads for Each Beam 21

4 Wave Speeds 24

5 Diffusion Parameters 29

6 Crack Depth Measurements by Technique 44

LIST OF FIGURES

1 Law of Refraction Illustrated 10
2 Waves Generated upon Impact 11
3 Tip Diffraction 11
4 Experimental Setup 12
5 Cross Section of Beams 18
6 Cross Sectional Analysis Problem 18
7 Load Setup 21
8 Flexural Cracks 21
9 Time of Flight Diffraction Measurement Setup 22
10 Signal at First and Second Transducers 23
11 Raw Wave Signals 24
12 Frequency Content of Impactor 25
13 Sample Output Signal 25
14 Diffusion Approximation Measurement Setup 26
15 Hann Window 27
16 Spectral Energy Density 27
17 Spectral Energy Density with Selected Window 28
18 Spectral Energy Density with Fitted Curve for a Cracked Section . . 28
19 Spectral Energy Density with ATME Illustrated 29
20 Crack Depth as a Function of ATME 29
21 Energy Evolution for Uncracked Beams 30
22 Finite Element Model 31
23 Example Crack Through Cross Section 33
24 Coring Details 33
25 Dyed Crack D 34
26 Depth as a Function of ATME for the Beam with #6 Bars 35
27 Energy Evolution for the Cracks on the Beam with #6 Bars 36

28 Comparison of the Estimation Methods on the Cracks on the Beam with #6 Bars 37

29 Depth as a Function of ATME for the Beam with #8 Bars 38

30 Energy Evolution for the Cracks on the Beam with #8 Bars 39

31 Comparison of the Estimation Methods on the Cracks on the Beam with #8 Bars 40

32 Depth as a Function of ATME for the Beam with #7 Bars 41

33 Energy Evolution for the Cracks on the Beam with #7 Bars 41

34 Comparison of the Estimation Methods on the Cracks on the Beam with #7 Bars 42

35 Comparison of the Estimation Methods on All of the Cracks 43

SUMMARY

Concrete is the most widely used construction material in the world, so the assessment of damage in concrete is critical from the point of view of both safety and cost. Of particular interest are macrocracks that extend through the concrete cover of the reinforcement, which can potentially expose the reinforcement to corrosive elements. The high density of scatterers such as aggregate and voids in concrete makes quantitative imaging with coherent ultrasound difficult. As an alternative, this research focuses on diffuse energy based ultrasonic methods rather than coherent ultrasonic methods for crack depth assessment. Two types of ultrasonic measurements were made on real cracks formed under four point bending: one that focuses on time of flight measurements from an impactor; while the other uses the arrival time of maximum energy in a diffuse field excited by an impulsive load from a transducer. Each of these ultrasonic techniques is used to interrogate a macro crack in a concrete beam, and the results are compared to determine their accuracy and robustness. The actual crack depth is determined using direct surface measurements and a destructive dye-injected approach with drilled cores. The results suggest that the diffusion method, using a maximum energy approach, more accurately estimates the crack than visual inspection and time of flight diffraction methods, which overestimate the depth.

CHAPTER I

INTRODUCTION

1.1 Motivation

In 2013, 75.1 million tons of Portland cement were produced in the United States, a figure that continues to rise each year [22]. This cement is used in concrete to produce the nation's growing infrastructure. Being able to evaluate damage in concrete is a critical issue from both safety and cost perspectives. Coherent ultrasonic methods have been found ineffective in concrete due to its high concentration of scatterers and heterogeneous nature, so a different approach is needed.

The type of damage this research is concerned with is cracking that reaches the reinforcement. Since reinforcement relies on the corrosion resistance of the alkaline concrete surrounding it, there is a threat of corrosion products developing on the reinforcement when a crack reaches the reinforcement. Corroding reinforcement causes a degradation of the tensile strength of the reinforcement and spalling of the concrete because corrosion products take up more volume than pure steel [25]. Preventive measures require the knowledge that cracks have reached the reinforcement, which requires more sophisticated techniques than visual inspection.

Several potential techniques have arisen as front-runners in the search for crack depth estimation in reinforced concrete: impact-echo, time of flight diffraction, diffusion approximation, and surface wave transmission.

1.2 Literature Review

1.2.1 Impact-Echo Method

The use of ultrasonics to evaluate damage in concrete is a relatively new concept that began in the 1980s, starting with the impact-echo technique, followed by the time of

flight diffraction technique, and finally leading to more advanced methods such as the diffusion approximation and surface wave transmission. Following the investigation of the collapse of several reinforced concrete structures in the 1970s, such as the collapse of the Skyline Plaza in 1973 [8], the National Institute of Standards and Technology (then the National Bureau of Standards) began to investigate nondestructive evaluation of concrete. Initially, evaluating the strength of concrete was the goal, since the Skyline Plaza collapsed due to the premature removal of shoring [8]. As research progressed, it became clear that ultrasonics could be used to assess other kinds of structural deficiencies in reinforced concrete.

Impact-echo method was investigated by Carino and Sansalone in 1984 for flaw detection in concrete using a single transducer in [7]. They found that the impact duration was crucial to the success of the technique In this study, they used the impact-echo technique to gauge the depth of flaws in the concrete. This hinged on knowing the pressure wave speed velocity in the concrete.

Sansalone and Carino later used the impact-echo technique to detect honeycombing, the depth of surface-opening cracks and ungrouted ducts [17]. Crack depths were determined by finding the peak in the frequency domain that corresponds with the reflection and diffraction between the top surface and the crack tip respectively. Although this technique can measure the crack depth accurately, it requires an experienced technician to determine which frequency peak corresponds with the crack.

1.2.2 Time of Flight Diffraction Method

In order to reduce the user bias, Sansalone et al. investigated time of flight techniques for depth determination of surface opening cracks in concrete [18]. They found that an α angle, the angle between the source/crack tip line and the crack tip/receiver line, of less than 45 degrees is ideal for making the P-wave arrival easy to identify. They also found that the depth estimation was insensitive to the impact duration.

The measured cracks were 16cm and 10cm deep, on specimens of 25cm x 1.8m x 1.8m. This study also showed that while the measurement technique worked for water-filled cracks, no information about partially grouted cracks could be determined. Inclined and curved cracks were found to be overestimated using this technique.

Wu et al. applied the time of flight diffraction technique to an EDM-formed crack in an aluminum plate and found a close agreement between the experimentally estimated crack depth and the actual crack depth [24]. Wu also compared the wave propagation in a plate with a normal surface-breaking crack to a prediction using a heterogeneous finite difference formulation and found them to be similar. Additionally, Wu found that the early signal shape depended upon the angle (α) between the source/crack tip line and the crack tip/receiver line. The EDM-formed cracks of depths between 2cm and 3cm were accurately interrogated.

Lin et al. applied the time of flight diffraction technique to surface-breaking cracks in concrete using two transducers instead of one [13]. They used both a time domain and a frequency domain analysis to estimate the crack depth through an assumed propagation path. In Lin's article, the crack depths range from 12cm to 24cm with specimens ranging from 30cm to 40cm deep.

Later Lin et al. examined the effectiveness of the time of flight diffraction technique on real cracks formed under four point bending in beams with tension, compression, and shear reinforcement [12]. The beams tested ranged from 25cm to 36cm deep, with crack depths of around 19cm. These crack depths were then validated using dye-injected cores. It was found that the depths estimated by the time of flight diffraction technique were within 1.6cm of the depth that the dye reached.

1.2.3 Surface Wave Transmission Method

The energy carried by a wave in an elastic medium is greatly impacted by the coupling conditions between the transducers and the elastic medium, which is not easily

measured or controlled. Angel and Achenbach numerically investigated the reflection and transmission of obliquely incident Rayleigh waves by a surface-breaking crack in 1984 [3]. This was a precursor to a self-calibrating technique using four transducers that create obliquely incident Rayleigh waves developed by Achenbach et al. in [2]. Using four transducers in a self-calibrating method, Achenbach et al. were able to accurately estimate the depth of an EDM-formed crack in an aluminum plate.

Popovics et al. investigated using the transmission of a surface wave across a crack to gauge the depth of the crack in concrete [14]. Popovics et al. used a slightly different self-compensating technique to eliminate the impact of coupling conditions. They still utilized four transducers, but in this case they were all colinear. The deeper a crack is, the greater the percentage of the wave amplitude that is reflected at the crack interface. This technique was found to be sensitive to cracks of a variety of depths as well as tightly closed cracks. Song et al. further investigated the same self-compensating technique and found that it was accurate at estimating crack depth in concrete [21].

Kee et al. took a different approach to avoiding the coupling condition issue; they used air-coupled transducers [11]. By eliminating contact, not only were they able to improve accuracy and repeatability, but also they were able to drastically increase the speed of testing. Current research has taken this same air–coupled approach for the above reasons.

Unfortunately, the surface wave transmission method requires a large amount of space on the concrete member to reduce near field effects near the crack. Additionally, the surface wave transmission method does not penetrate more than about one wavelength into the concrete due to the exponential decay of Rayleigh waves with increasing depth. This means that this method will not be as useful when measuring deeper cracks.

1.2.4 Diffusion Method

Weaver and Sachse applied the diffusion approximation to glass beads in water to compare the diffusion parameters from a theoretical standpoint to those obtained from a curve fit to the experimental data [23]. They used a 3D unbounded analytical solution to the diffusion approximation to recover the diffusion parameters, which did not match well with theoretical values, but did result in a predicted energy evolution curve that matched the experimentally measured energy evolution very well. They found that diffusivity had a heavy dependence on frequency. The dissipation rate was found to be greater than expected based on a model of viscous shear loss at solid/liquid interfaces.

Diffusion method was first applied to cementitious materials by Anugonda and Turner using a 1D analytical solution to the diffusion approximation [5]. Anugonda and Turner showed that diffusion parameters such as diffusivity and dissipation can be obtained from a curve fit to the measured energy curve in cementitious materials. Like Weaver and Sachse, Anugonda and Turner noticed that diffusivity depended on frequency. Although none of the specimens tested contained any intentional damage in them, Anugonda and Turner posited that distributed microcracking consistent with early stages of damage would result in a lowered diffusivity value. At this point the primary usefulness for diffuse-field ultrasonics was characterization of microstructural damage as opposed to macrostructural damage.

Becker investigated the effects of aggregate size on the diffusion parameters by casting mixtures of cement and glass beads of varying sizes [6]. Dissipation was found to be roughly the same for each glass bead size, but diffusivity was lower in the larger glass bead sizes, indicating an increased amount of scattering. Becker also pointed out the value of separating material attenuation (i.e., dissipation) from the scattering loses (i.e., diffusivity).

The diffusion approximation was also investigated by Deroo et al. as a method

for gauging two types of microstructural damage in concrete: alkali-silica reaction and thermal damage [10]. They found that the diffusivity decreased with increasing damage, but dissipation remained relatively constant. They also noted that the 3D infinite solution to the diffusion equation resulted in smaller error than the 3D bounded solution, due to the higher computational requirements of the 3D bounded solution.

Diffuse-field ultrasonics were first used to detect and quantify macroscopic damage in concrete by Ramamoorthy et al. in [16]. They compared the arrival time of maximum energy in a cracked section to that of an uncracked section to obtain the time delay due to the crack. The arrival time was compared to a numerical solution for peak arrival time as a function of distance from the source. Cracks ranging from 1.27cm to 7.62cm were accurately estimated on slabs 61cm x 61cm x 20cm. These cracks were formed using a plate cast into the concrete and removed before the concrete reached full strength. They showed that this analysis can accurately measure the depth of cracks in unreinforced concrete.

Seher et al. developed a finite element model to numerically calculate the arrival times of maximum energy (ATME) for varying crack depths and configurations in [19]. Specimens with notches of 2.5cm and 10.2cm were cast to validate these finite element models. The finite element models were found to accurately describe the evolution of energy over time. Finite element models for partially closed cracks and two parallel cracks were also investigated, but neither was found to be effective at uniquely quantifying the crack depths. Finally, rebar was found, numerically, to have no noticeable effect on the arrival time of maximum energy.

Quiviger et al. investigated the effect of a macrocrack in concrete on the diffusion parameters [19]. In these tests, two series of specimens of 15cm x 15cm x 60cm dimensions were used. One of these series had notches, while the second included notches that served as crack initiation sites under four point bending. It was found

that the dissipation did not vary considerably with crack depth, but the diffusivity decreased with greater crack depths [19].

1.3 Objective

This research examines the applicability of the diffusion approximation and the time of flight diffraction techniques to gauge crack depths on real cracks on reinforced concrete beams. By comparing the two techniques side by side, recommendations can be made as to where to focus future research for a device for field testing.

CHAPTER II

THEORETICAL BACKGROUND

2.1 Wave Propagation in Elastic Media

2.1.1 Derivation of Law of Motion

The wave equation for the propagation of elastic waves in an elastic medium is derived using three equations: the homogeneous equation of motion in equation (1), the definition of the strain tensor in equation (2), and the stress-strain relationship for isotropic solids in equation (3) [1]. These equations assume that the elastic medium is isotropic, homogeneous, and that displacements are small ($sin(\theta) \approx \theta$).

$$\rho \frac{\partial^2 u_i}{\partial t^2} = \partial_j \tau_{ij} \tag{1}$$

$$e_{ij} = \frac{1}{2}(\partial_i u_j + \partial_j u_i) \tag{2}$$

$$\tau_{ij} = \lambda \delta_{ij} e_{kk} + 2\mu e_{ij} \tag{3}$$

In equations (1–3), ρ is the density of the elastic medium, τ_{ij} is the stress on the face perpendicular to the i direction in the j direction, u_i is the displacement in the i direction, and λ and μ are the Lamé constants.

$$\mu \bigtriangledown^2 u + (\lambda + \mu) \bigtriangledown \bigtriangledown \cdot u = \rho \ddot{u} \tag{4}$$

One solution to the wave equation is a harmonic wave of the form in equation (5).

$$u(x,t) = Acos[\omega(\frac{x}{c} - t)] \tag{5}$$

In equation (5), A is the amplitude and $\omega = 2\pi f$, where f is the frequency of the harmonic wave.

The partial differential wave equation can be uncoupled using Helmholtz decomposition using potential functions [1]. The solution for the wave equation becomes equation (6).

$$u = \bigtriangledown\phi + \bigtriangledown \times \psi \tag{6}$$

Using this decomposition, the wave equation is split into two separate wave equations as seen in equations (7) and (8).

$$\bigtriangledown^2\phi = \frac{1}{C_p^2}\ddot{\phi} \tag{7}$$

$$\bigtriangledown^2\psi = \frac{1}{C_s^2}\ddot{\psi} \tag{8}$$

This leads to two kinds of waves, a longitudinal wave and a shear wave. The velocity of both wave types can be written as a function of the Lamé parameters. C_p is the velocity of the pressure wave and C_s is the velocity of the shear wave.

$$C_p^2 = \frac{\lambda + 2\mu}{\rho} \tag{9}$$

$$C_s^2 = \frac{\mu}{\rho} \tag{10}$$

Finally, the Lamé parameters can be written in terms of other more common material properties, E, the Young's modulus, and ν, Poisson's ratio. These relationships are shown in equations (11) and (12).

$$\lambda = \frac{E\nu}{(1+\nu)(1-2\nu)} \tag{11}$$

$$\mu = \frac{E}{2(1+\nu)} \tag{12}$$

2.1.2 Law of Refraction

At interfaces between materials, such as the interface between cement paste and aggregate, elastic disturbances are reflected and transmitted. Waves are not just reflected and transmitted at interfaces; a phenomenon called mode conversion also

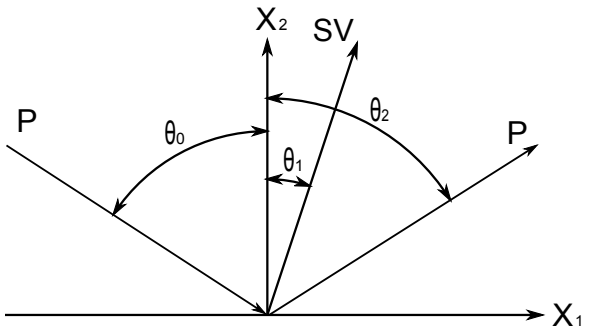

Figure 1: Law of Refraction Illustrated

occurs. In wave conversion, the incident wave is reflected and transmitted as both longitudinal waves and shear waves, regardless as to which the incident wave is. Since longitudinal and shear waves have different velocities in an elastic medium, in order to satisfy boundary conditions, the angle of incidence is not always the resulting angle. This is best seen in figure 1.

In figure 1, P is the incident longitudinal wave and the reflected longitudinal wave and SV is the reflected shear wave.

These angles can be calculated based on the angle of the incident wave using the relationship in equation (13), frequently referred to as Snell's Law of Reflection and Descartes' Law [1]. This relationship is derived by assuming that horizontal slowness ($\frac{\Delta t}{\Delta x}$) remains constant at the interface.

$$k_0 sin(\theta_0) = k_1 sin(\theta_1) = k_2 sin(\theta_2) \tag{13}$$

In equation (13), k_0, k_1, and k_2 represent the wave speeds of the waves in question and θ_0, θ_1, and θ_2 represent their corresponding angles relative to the direction normal to the interface.

This phenomenon explains the scattering events that make a diffuse field. These interfaces can be found at every aggregate and void, which causes the ballistic signal to reflect throughout the concrete.

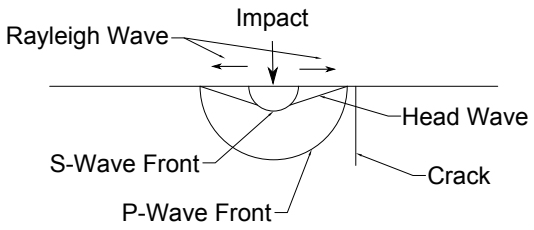

Figure 2: Waves Generated upon Impact

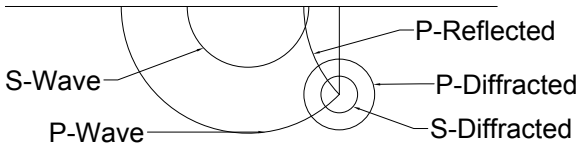

Figure 3: Tip Diffraction

2.2 Time of Flight Diffraction

2.2.1 Background

A transient disturbance, such as an impact from a hammer or signal from a transducer, propagates throughout a solid in the form of elastic waves. Spherical longitudinal (P) and shear (S) waves radiate out from the point of impact and Rayleigh (R) surface waves radiate outward from the point of impact along the surface, as seen in figure 2. A head wave (H) is also generated between the P and S waves to satisfy the boundary conditions at the free surface [1]. When the P and S waves strike the tip of the crack, the tip acts as a new source for diffracted P and S waves, as seen in figure 3 [18].

By placing a transducer on the opposite side of the crack, the arrival time of the P wave at the opposite side of the crack can be measured. The time of impact can be measured by timing how long it takes the R wave to travel a known distance from the impact. This set up can be seen in figure 4.

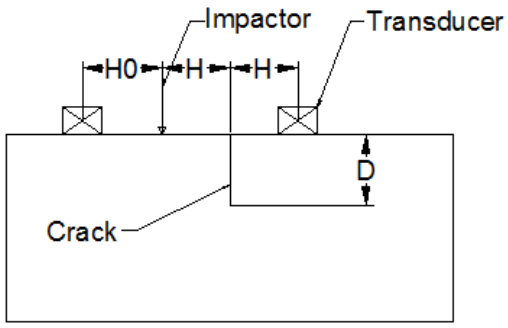

Figure 4: Experimental Setup

2.2.2 Derivation of the depth equation

Once the longitudinal wave velocity, C_p, is known, the distance traveled by the wave is calculated using equation (14).

$$\Delta x = C_p \Delta t \tag{14}$$

By assuming a perpendicular crack and equal distances from impactor to crack and from crack to receiving transducer, an isoceles triangle is formed with crack tip, impact site, and receiving site forming the vertices. The two legs must add up to the total distance traveled by the wave, Δx, meaning each leg must equal $\Delta x/2$. The depth of the crack is then related to Δx and the distance from the crack to the receiving transducer, H, using the Pythagorean theorem as shown in equation (15).

$$D^2 + H^2 = (\frac{\Delta x}{2})^2 \tag{15}$$

Solving this equation for D yields equation (16) in terms of longitudinal wave speed, C_p, distance from crack to receiving transducer, H, and time of flight, Δt [13].

$$D = \sqrt{(\frac{C_p \Delta t}{2})^2 - H^2} \tag{16}$$

2.3 Diffusion Approximation

2.3.1 Background

The diffusion equation has its roots in the study of electromagnetic wave phenomena [19]. As with elastic waves, when in the presence of many scatterers on the same order of magnitude as the wavelengths, electromagnetic waves quickly become scattered and data processing techniques that focus on the individual waves become difficult. This difficulty prompted research into an energy based evaluation of diffuse fields. Unfortunately, elastic wave fields are more complex than electromagnetic wave fields because of the polarization of elastic waves. This issue is dismissed by the key assumption that once a field is diffuse, it has lost all coherence in space or time [19]. This assumption means that instead of considering the displacements due to the superimposed individual waves, the system can be modeled purely with an energy-based model.

2.3.2 Derivation of the Diffusion Equation

There are a few more assumptions made in the formulation of the diffusion equation related to the treatment of energy. First of all, it is assumed that scattering events are perfectly elastic, meaning that no energy is lost during a scattering event [6]. Second, it is assumed that the high impedance mismatch at the boundary will result in negligible energy leaking to the surrounding air [6]. Lastly, the medium is assumed to be isotropic, which means that energy will travel in the same manner in every direction [6]. With those assumptions, the diffusion equation can be derived either by using a random walk model or by considering ultrasonic diffusion a quantum mechanical problem [19]. A more in depth treatment of the derivation can be found in [20]. The diffusion equation turns out to be the second order parabolic partial differential equation found in equation (17).

$$\frac{\partial\langle E(\mathbf{x},t,f)\rangle}{\partial t} - D\Delta\langle E(\mathbf{x},t,f)\rangle + \sigma\langle E(\mathbf{x},t,f)\rangle = P(\mathbf{x},t,f) \tag{17}$$

In equation (17) $\langle E(\mathbf{x}, t, f)\rangle$ is the expected value of the spectral energy density as a function of location, time, and frequency. $P(\mathbf{x}, t, f)$ is the forcing term for the equation, which describes how the medium is excited. D is the diffusivity coefficient, which is the rate of diffusion of the ultrasonic field. σ is the dissipation coefficient, which characterizes the rate of loss of energy.

2.3.3 Solutions to the Diffusion Equation

2.3.3.1 One Dimensional Bar Solution

It is assumed that the bar is much longer than it is thick ($t << L$) so that it can be approximated as a 1D problem. The forcing function is an impulse at the origin as seen in equation (18).

$$P(\mathbf{x}, t, f) = P_0\delta(t)\delta(\mathbf{x}) \tag{18}$$

There is no energy flux across the boundaries as seen in equation (19).

$$\frac{\partial\langle E(0, t, f)\rangle}{\partial x_1} = 0 \tag{19}$$

There is initially no energy in the sample as seen in equation (20).

$$\langle E(\mathbf{x}, 0, f)\rangle = 0 \tag{20}$$

This all leads to the following simplified partial differential equation as seen in equation (21).

$$\frac{\partial\langle E(\mathbf{x}, t, f)\rangle}{\partial t} - D\frac{\partial^2\langle E(x_1, t, f)\rangle}{\partial x_1^2} + \sigma\langle E(x_1, t, f)\rangle = P(x_1, t, f) \tag{21}$$

Equation (21) is a simple inhomogeneous heat conduction equation with lower order terms and Neumann boundary conditions [15]. It can be solved using a change of function followed by separation of variables to get the following solution in equation (22) [10].

$$\langle E(x_1, t, f)\rangle = \frac{P_0}{2\sqrt{D\pi t}}e^{-\frac{x_1^2}{4Dt}}e^{-\sigma t} \tag{22}$$

2.3.3.2 Two Dimensional Bounded Domain Solution

For a 2D bounded domain, it is assumed that the space is spanned by dimensions x_1 and x_2. The forcing function is an impulse at x_0 as seen in equation (23).

$$P(\mathbf{x}, t, f) = P_0\delta(t)\delta(\mathbf{x} - \mathbf{x_0}) \tag{23}$$

The gradient of the energy function in the x_3 direction is assumed to be 0 as seen in equation (24).

$$\frac{\partial\langle E(0, t, f)\rangle}{\partial x_3} = 0 \tag{24}$$

There is no energy flux across the boundaries as seen in equations (25) and (26).

$$\frac{\partial\langle E(\mathbf{x}, t, f)\rangle}{\partial x_1} = 0 \text{ for } x = 0, l \tag{25}$$

$$\frac{\partial\langle E(\mathbf{x}, t, f)\rangle}{\partial x_2} = 0 \text{ for } x = 0, d \tag{26}$$

In equations (25) and (26) l and d are the length and depth of the domain respectively. Finally, there is initially no energy in the sample as seen in equation (27).

$$\langle E(x, 0, f)\rangle = 0 \tag{27}$$

These conditions lead to the following simplified partial differential equation seen in equation (28).

$$\frac{\partial\langle E(\mathbf{x}, t, f)\rangle}{\partial t} - D\{\frac{\partial^2\langle E(x_1, t, f)\rangle}{\partial x_1^2} + \frac{\partial^2\langle E(x_2, t, f)\rangle}{\partial x_1^2}\} + \sigma\langle E(x_1, t, f)\rangle = P(x_1, t, f) \tag{28}$$

Equation (28) is a simple inhomogeneous heat conduction equation in 2 dimensions with Neumann boundary conditions. Its solution is equation (29) [19].

$$\begin{aligned}\langle E(\mathbf{x},t,f)\rangle = \quad & \left\{1+\sum_{n=1}^{\infty}2\cos\left(\frac{n\pi x_{1,0}}{l}\right)\cos\left(\frac{n\pi x_1}{l}\right)e^{-D(\frac{n\pi}{l})^2 t}\right. \\ & +\sum_{m=1}^{\infty}2\cos\left(\frac{m\pi x_{2,0}}{p}\right)\cos\left(\frac{m\pi x_2}{p}\right)e^{-D(\frac{m\pi}{p})^2 t} \\ & +\sum_{n=1}^{\infty}\sum_{m=1}^{\infty}4\cos\left(\frac{n\pi x_{1,0}}{l}\right)\cos\left(\frac{n\pi x_1}{l}\right)\cos\left(\frac{m\pi x_{2,0}}{p}\right)\cos\left(\frac{m\pi x_2}{p}\right) \\ & \left.\times e^{-D[(\frac{n\pi}{l})^2+(\frac{m\pi}{p})^2]t}\right\}\times P_0 e^{-\sigma t}\end{aligned} \tag{29}$$

In equation (29), $x_{1,0}$ and $x_{2,0}$ are the coordinates of the impulse, and x_1 and x_2 are the coordinates of the receiver.

Although other analytical solutions exist (3D cuboid, 3D unbounded, 3D bounded, and more), Deroo et al. found that the 2D bounded solution is the best compromise between accuracy and computing time [10] .

CHAPTER III

EXPERIMENTAL PROCEDURE

3.1 Specimen Preparation

3.1.1 Specimen Design

Reinforced concrete beams are cast as samples for natural cracks. Three beams, 2.4m in length with a 25.4cm x 15.2cm cross-section, contain two identically sized bars placed at 3.2cm from the tension surface as seen in figure 5. The rebar sizes of #6, #7, and #8 are used to promote a range of crack depths. Cross sectional analysis is performed to give conservative estimates for crack depths and cracking moment. This is a simple force balance problem as posed in figure 6.

This formulation assumes plane sections remain plane, the compression block has a triangular distribution, the stress-strain relationship is linear, the load is applied quasi-statically, and the tensile capacity of the concrete is negligible. The Young's modulus of the steel is assumed to be 200GPa and the Young's modulus of the concrete is calculated according to ASTM C39/C39M - 12a to be 24.2GPa.

In figure 6, c is the depth of the compression block, d is the distance from the compression surface to the centroid of the reinforcement, b is the width of the beam, ϵ_c is the strain at the compression surface, ϵ_s is the strain at the centroid of the rebar, f_c is the stress in the outer compression fiber, f_s is the stress at the centroid of the rebar, C is the resulting compressive force carried by the concrete, and T is the resulting tensile force carried by the rebar.

To solve this cross section problem, first the compressive and tension forces are written in terms of stress and cross sectional areas, as seen in equations (30) and (31).

$$C = \frac{1}{2} f_c b c \tag{30}$$

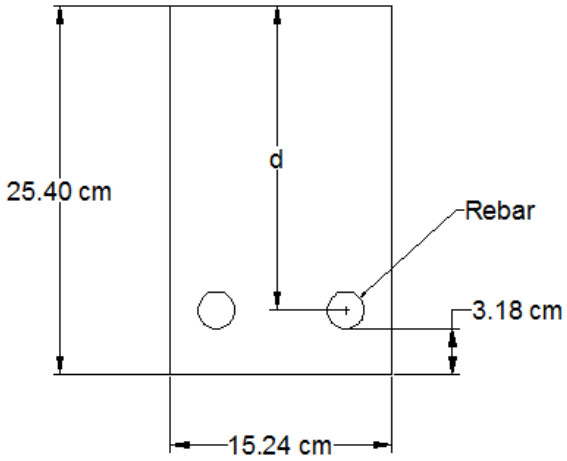

Figure 5: Cross Section of Beams

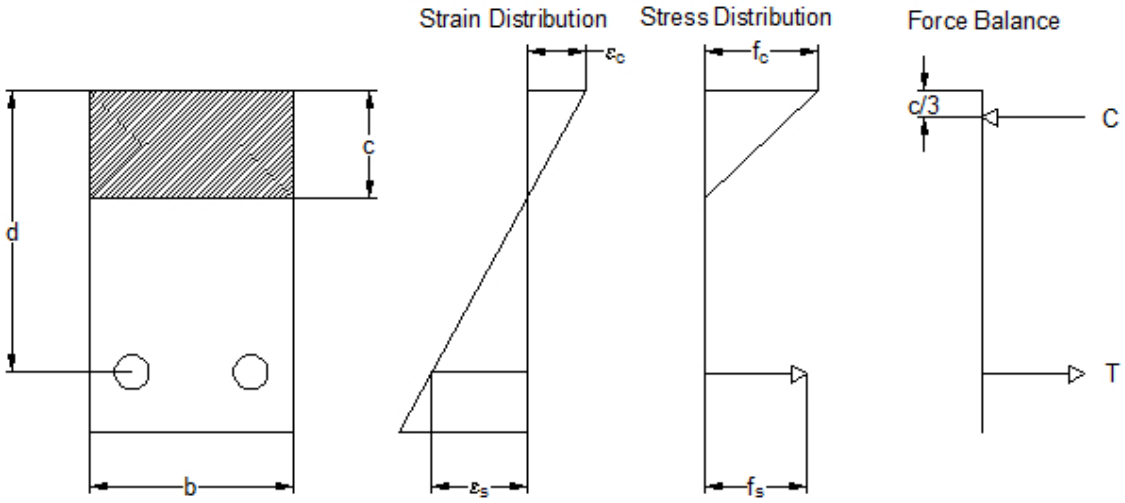

Figure 6: Cross Sectional Analysis Problem

$$T = A_s f_s \tag{31}$$

In equations(30) and (31), A_s is the cross sectional area of the rebar. Since the stresses are not directly related (as seen in figure 6), the stresses are rewritten in terms of strain using Hooke's Law.

$$f_s = E_s \epsilon_s \tag{32}$$

$$f_c = E_c \epsilon_c \tag{33}$$

Since it is assumed that plane sections remain plane, the strain can be easily related using similar triangles to obtain the relationship between the strain in the compression face and the strain in the steel seen in equation (34).

$$\epsilon_s = \frac{d - c}{c} \epsilon_c \tag{34}$$

In order for the beam to be in equilibrium, the compressive and tensile forces must sum to zero. A summation of the forces along the length of the beam results in equation (35).

$$C = T \tag{35}$$

Finally, substituting (30) and (31) into (35) yields (36), a quadratic equation with a single unknown, c. The quadratic equation is then used to find two values for c: one which is outside the beam's dimensions and thus ignored, and one that is the distance from the compression face to the centroid of the cross section.

$$E_c b c^2 + 2 A_s E_s c - 2 A_s E_s d = 0 \tag{36}$$

The theoretical estimate for crack depth is simply the total height of the beam less the value of c. Table 1 contains the important values for each beam cast.

In reality, these theoretical crack depths are conservative because the concrete does have some tensile capacity, the loading is not quasi-static, and the crack does not open along a perfectly straight path.

Table 1: Beam Details

Rebar Size	A_s (mm^2)	d (cm)	c (cm)	Theoretical Crack Depth (cm)
#6	568	21.91	8.95	16.45
#7	774	21.75	9.95	15.45
#8	1018	21.59	10.86	14.54

Table 2: Compressive Strength of Concrete

Compressive Strength (MPa)	25.12
Standard Deviation (MPa)	2.93

3.1.2 Material Properties

The concrete mix, provided by Vulcan Atlanta, was produced from Type I/II cement with #57 stone.

Concrete cylinders were cast from the same pour as the beams and later tested to determine the compressive strength of the concrete. The specimens were 7.6cm in diameter and 12.7cm in length. In accordance with ASTM C39/C39M - 12a, the load rate stayed between 0.20MPa/s and 0.30MPa/s. The average compressive strength and standard deviation can be found in table 2.

3.1.3 Loading

The beams were allowed to cure for 28 days before the surface is prepared for testing by grinding. The beams were cracked in four point bending as seen in figure 7. This setup resulted in evenly spaced cracks on each beam as can be seen in figure 8.

The beams are loaded in four point bending, the loads were applied evenly to the two roller bearings on the top sides of the concrete beams. The concrete beams were supported by roller supports positioned as seen in figure 7. This loading was designed to create an area of constant moment between the two supports. The maximum moment applied to the middle section of the beam can be found in table 3.

Ultrasonic testing is done after the beams have been unloaded.

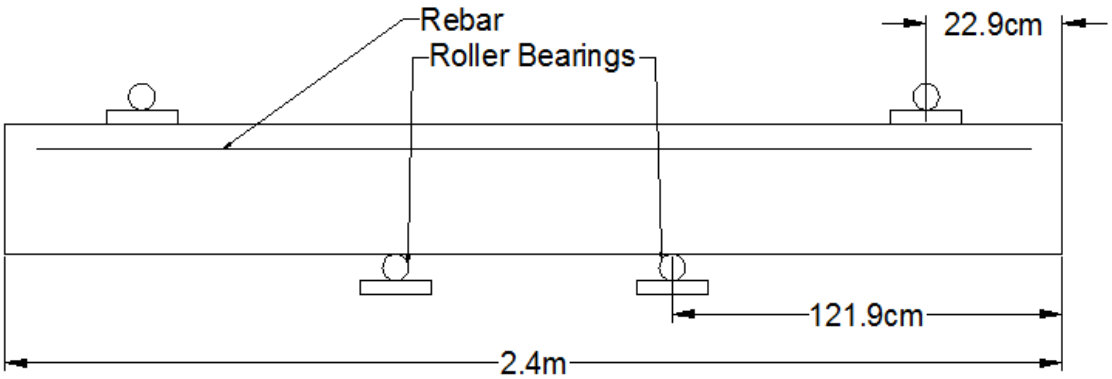

Figure 7: Load Setup

Figure 8: Flexural Cracks

Table 3: Maximum Loads for Each Beam

Rebar Size	Maximum Load (Nm)
# 6	19.52
# 7	16.98
# 8	17.00

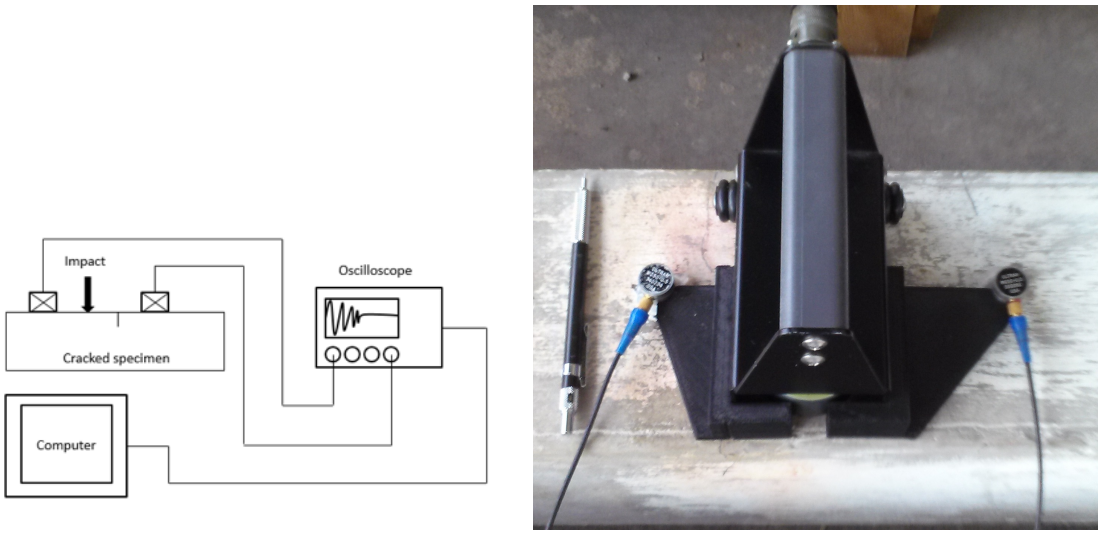

(a) Measurement Schematic (b) Transducer Placement

Figure 9: Time of Flight Diffraction Measurement Setup

3.2 Time of Flight Diffraction

3.2.1 Instrumentation

Transient elastic waves are introduced to the specimen via a commercially available Olson impact echo impactor. Two Ultran WC50-0.5 transducers along with a Tektronix TDS 5034 Digital Phosphor Oscilloscope are used to record data. The measurement setup is shown in figure 9a. The placement of the transducers on the beam using fixtures can be seen in figure 9b. The impactor was placed 3.8cm from the crack on one side and the receiving transducer was also placed 3.8cm away from the crack on the opposite side in line with the impactor. The Rayleigh receiver was placed 10.2cm away from the crack on the impactor side of the crack.

3.2.2 Data Processing

3.2.2.1 Starting Point Algorithm

The starting times of each signal are identified through a computer algorithm, to eliminate user bias. This computer algorithm traverses the signal from start to finish and marks the first time when the signal exceeds 70% of the maximum value of the

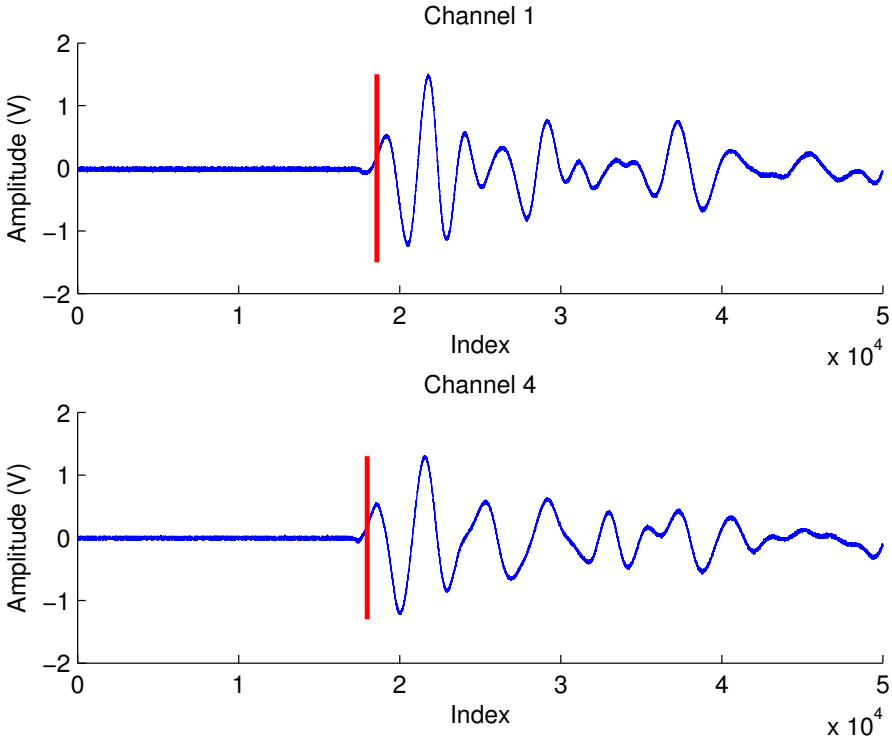

Figure 10: Signal at First and Second Transducers

signal; this function runs again using this point as the new endpoint of the signal. The vertical red lines in figure 10 denote the starting points selected by the algorithm for sample signals.

3.2.2.2 Wave Speed Measurement

Before any time of flight diffraction data can be processed, it is necessary to know the speed of the Rayleigh and longitudinal waves that are introduced with an impact. The Rayleigh wave speed can be found by calculating the difference in arrival time of the wave at two transducers set a known distance apart. The wave speed is simply the separation distance divided by difference in arrival times.

The longitudinal wave speed is more difficult to measure directly using the same instrumentation as the time of flight diffraction and diffusion approximation, so an approximate method is used. This method takes advantage of the resonant frequency

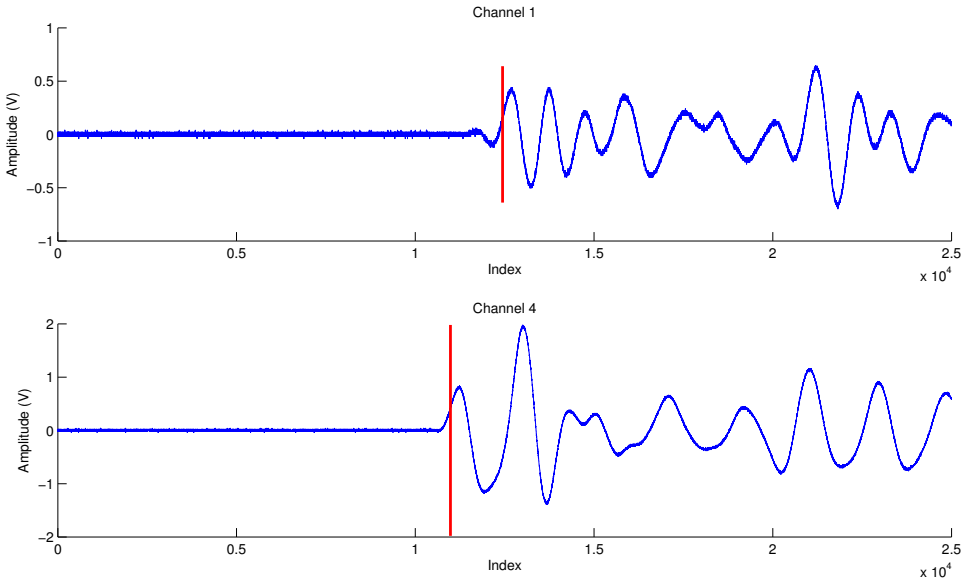

Figure 11: Raw Wave Signals

Table 4: Wave Speeds

Rebar Size	C_p (m/s)	C_r (m/s)
#6	4031	1697
#7	4040	1701
#8	4257	1732

of the material based on the thickness of the beam.

$$C_p = \frac{2hf}{\beta} \tag{37}$$

In equation (37), C_p is the longitudinal wave speed, h is the thinnest dimension of the beam, f is the resonant frequency, and β is a constant equal to 0.96.

The measured wave speeds for each beam are tabulated in table 4.

3.2.2.3 Depth Estimation

The time of impact, t_0, is calculated using equation (38). Finally, Δt is calculated by subtracting t_4 from t_0 and plugged into equation (16) to estimate the crack depth.

$$t_0 = t_1 - \frac{H_0}{C_r} \tag{38}$$

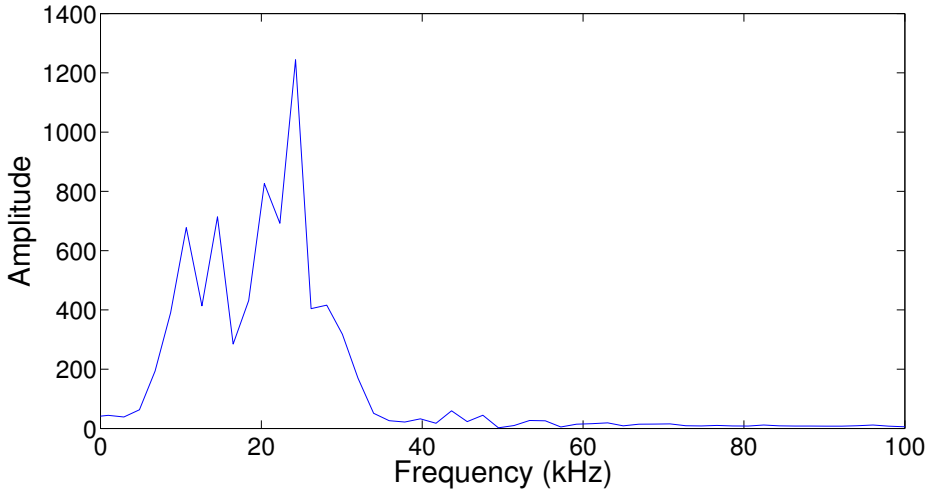

Figure 12: Frequency Content of Impactor

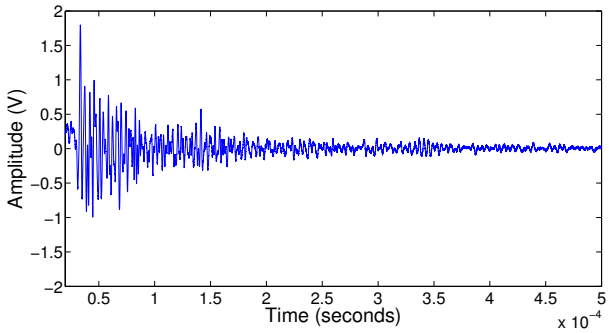

Figure 13: Sample Output Signal

3.3 Diffusion Approximation

3.3.1 Instrumentation

A Tektronix TDS 5034 Digital Phosphor Oscilloscope was used to record the ultrasonic signal. A Panametric Model 5072 PR Pulser/Receiver was used in concert with a Digital Wave amplifier to generate a sinusoidal pulse and receive the resulting output signal. The transmitting transducer was an Ultran WC50-0.5 transducer. A sample output signal is found in figure figure 13.

One of the key features of a diffuse field is that when spatially averaged it approaches zero, so the receiving transducer was an Ultran CC500-D13 transducer modified with an aluminum cone to approximate a point receiver, which reduces this spatial

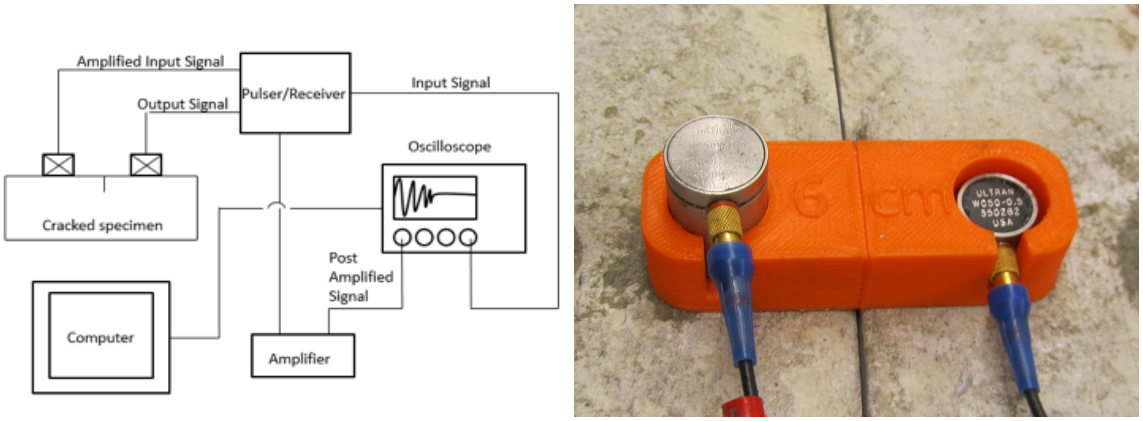

(a) Measurement Schematic (b) Transducer Placement

Figure 14: Diffusion Approximation Measurement Setup

averaging effect. The average of 1000 acquisitions was used for a better signal to noise ratio.

Measurements are taken with transducers separated by 6cm. Figure 14a shows the data acquisition schematic. Figure 14b shows the placement of the transducers relative to the crack.

3.3.2 Diffuse Data Processing

The received signal on an uncracked section is compared to the 2D bounded solution of the diffusion equation to obtain the values for diffusivity (D) and dissipation (σ) of the concrete, using the following steps.

1. Divide the signal into segments that overlap by 90%. The length of the segments is calculated by dividing the total signal length by the sampling period.

2. Compute the short-time Fourier transform to calculate the spectrogram at the frequencies specified in step 1. Using the spectrogram(...) function built into MATLAB will also provide the power spectral density of each segment. Each segment is also multiplied by the Hann window inside the spectrogram(...) function to reduce the artificial side lobes. The Hann window is shown in figure 15.

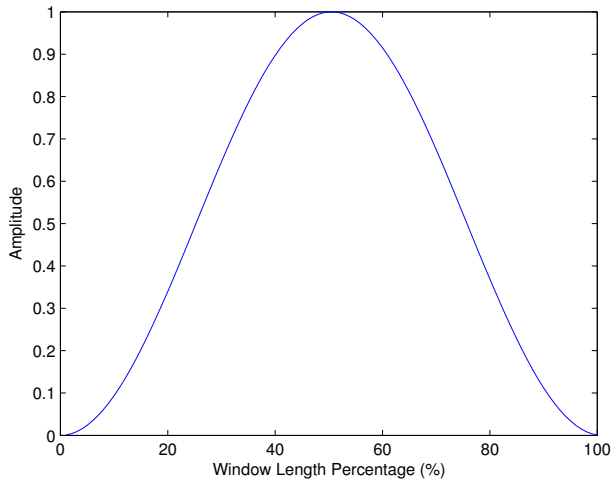

Figure 15: Hann Window

3. Integrate the power spectral density for the given frequencies using the cumtrapz(...) MATLAB function, which applies the trapezoidal rule, to obtain the spectral energy density as a function of time. In this research, the chosen frequency range was from 450kHz to 550kHz. The spectral energy density plot can be seen in figure 16.

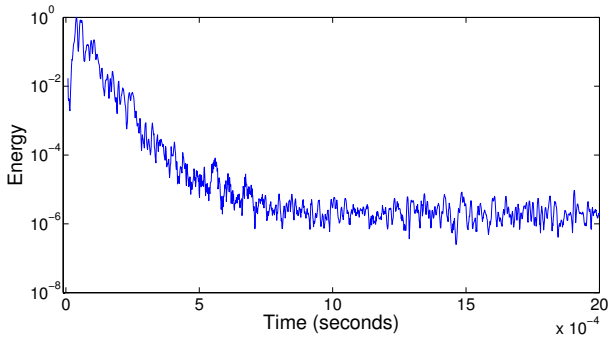

Figure 16: Spectral Energy Density

4. Repeat steps 1 through 4 on a cracked section of the beam. Plot the spectral energy density as a function of time and select a window that only includes the portion of the signal that is above the noise level, as shown in figure 17. This is the only time when user bias can drastically influence the results.

5. Use the lsqnonlin(...) function in MATLAB to fit a curve to both the uncracked

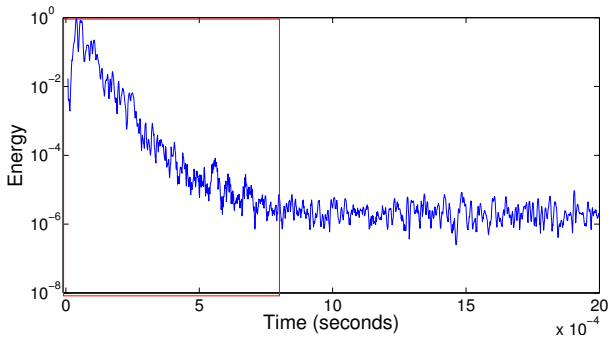

Figure 17: Spectral Energy Density with Selected Window

energy plots and cracked energy plots. The uncracked energy plot can be seen in figure 18. Diffusivity and dissipation values for the concrete are recovered from the parameters of the fitted curve.

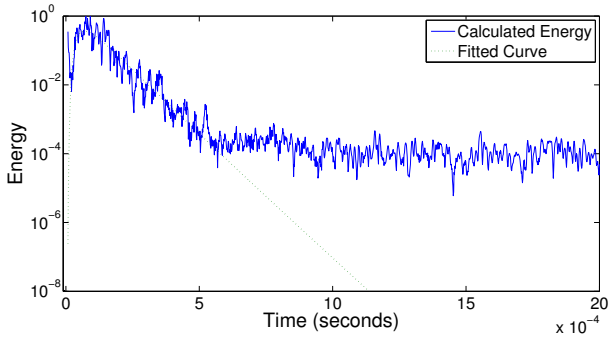

Figure 18: Spectral Energy Density with Fitted Curve for a Cracked Section

6. Extract the arrival time of maximum energy (ATME) by finding the time value that corresponds to the maximum of the fitted curve of the cracked energy plots. The ATME is pointed to on figure 19.

7. The diffusion value is used in a finite element method heat transfer model, like one investigated in [19], to obtain a relationship between the ATME and crack depth, as seen in figure 20.

8. Using the energy data as a function of time obtained from the finite element simulation, multiply each point's energy value by its corresponding dissipation term, $e^{-\sigma t}$, as found in equation (29).

9. Calculate the adjusted arrival time based on the comparison between the

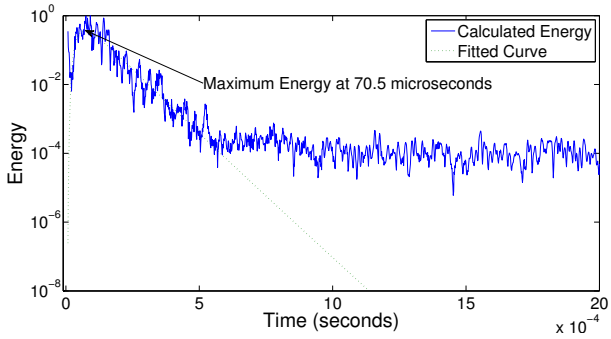

Figure 19: Spectral Energy Density with ATME Illustrated

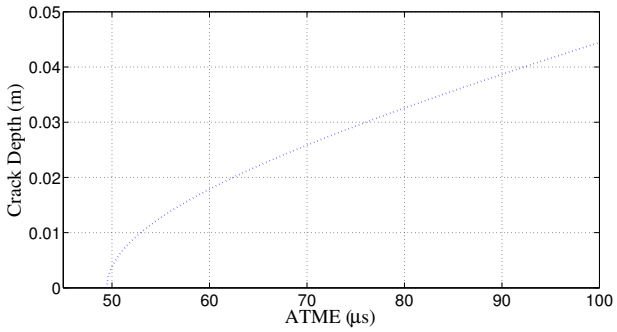

Figure 20: Crack Depth as a Function of ATME

uncracked ATME and finite element energy curve.

10. Using the ATME found in step 8, find the corresponding point in figure 20 to obtain the estimated crack depth.

The evolution of energy in an uncracked portion of each beam is calculated using the process described above to obtain figure 21.

The recovered diffusivity parameters are in table 5. They are similar to those found in [19].

These parameters are used as inputs in the finite element simulation to yield a

Table 5: Diffusion Parameters

Rebar	Diffusivity (m^2s^-1)	Dissipation (s^-1)
# 6	9.75	17970
# 7	7.91	22853
# 8	5.04	21519

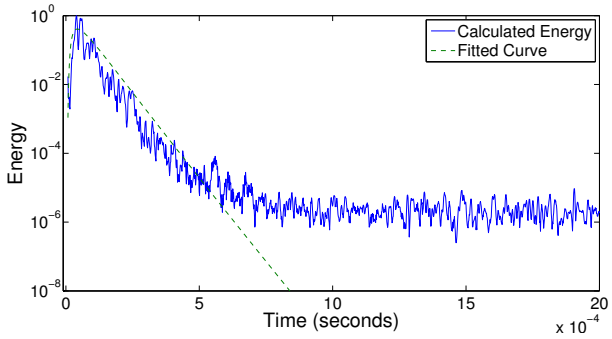

(a) Beam with #6 Bars

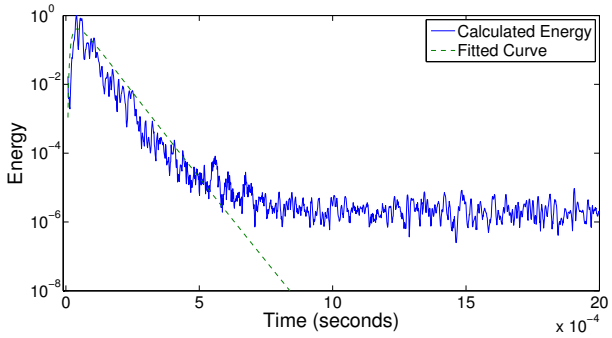

(b) Beam with #8 Bars

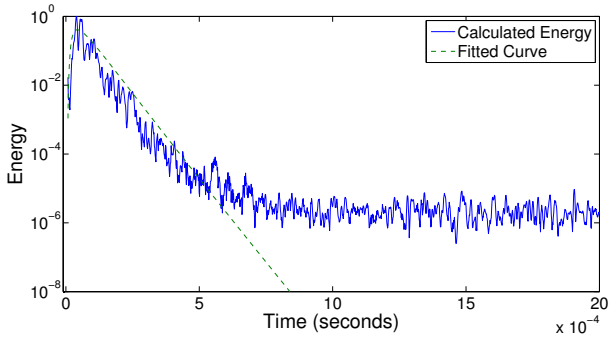

(c) Beam with #7 Bars

Figure 21: Energy Evolution for Uncracked Beams

relationship between the arrival time of maximum energy and the depth of the crack found in the Results section.

3.3.3 Finite Element Model

Although the diffusion equation has a few analytical solutions, when cross section geometry gets more complex than the simple rectangular prisms investigated in this research, a different method must be used to obtain a theoretical solution. Finite element analysis is a method for discretizing complex geometries into elements that have assumed field properties. For example, in heat conduction problems, each element has an assumed heat field. In this research, finite element analysis is used to simulate the conduction of heat through a beam with a crack. More details on finite element formulation and uses can be found in [9].

A two-dimensional finite element model was parametrically discretized by 4-node bilinear quadrilateral elements with one degree of freedom per node. 6000 Plane55 element in ANSYS was found to be the ideal type and number of elements that yields the best compromise between accuracy and computation time in [19]. More information regarding the Plane55 element can be found in [4]. A sample mesh can be seen in figure 22.

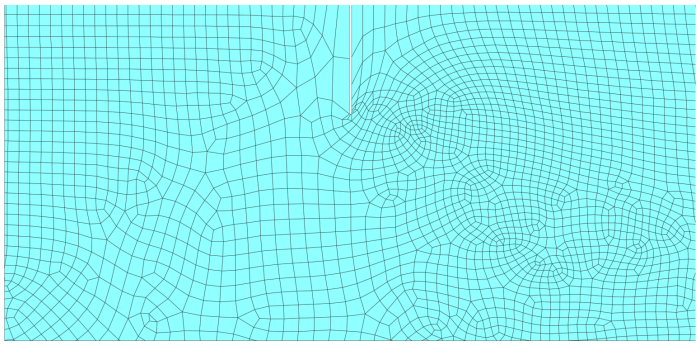

Figure 22: Finite Element Model

The crack was modeled as a thin rectangle (1mm thick) of varying depth. A transient heat conduction simulation is run using an impulse excitation at the location

of the source with a duration of $0.1\mu s$. The mass density and specific heat capacity were both set to one, and the thermal conductivity is set to the diffusivity, D, found in step 5 above.

The amplitude of the heat source impulse also does not impact the ATME, so a magnitude of one is used. The dissipation is accounted for in step 8 above, so it is not used as an input to the finite element simulation.

3.4 Crack Depth Validation

To provide a ground truth measurement of crack depth, dye is injected into the cracks and then a core is drilled containing the dye-injected crack. The dye is an acetone-based dye composed of 5g of powdered dye and 75g of acetone, thoroughly mixed. Dye is injected into cracks D and H using an acetone-based dye forced into the crack with 400kPa using the device shown in figure 24a. The device is affixed to the concrete beam using a combination of metal/concrete 2-part epoxy and two bar clamps. The pressure is applied through the Schrader valve, seen at the top of the injection device, via a hand pump with a pressure indicator.

After dye was injected, a 6.35cm diameter core is drilled to determine how deep the dye reached. Theoretically, the crack is the same depth throughout the cross section of the beam, however in practice, the crack depth varies across the cross section. A schematic of this variation is depicted in figure 23. To counteract this complication, the coring bit is positioned so that the outer edge of the core corresponds with the location, across the width of the beam, where the ultrasonic equipment was placed. This coring setup can be seen in figure 24b.

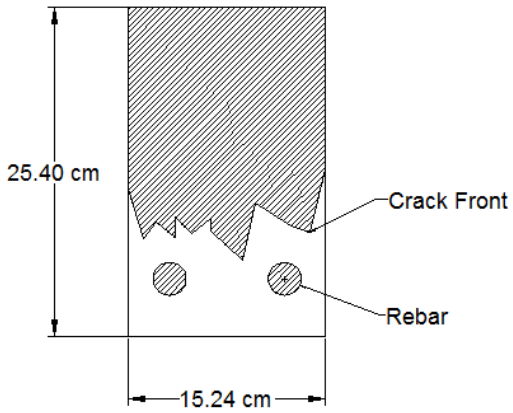

Figure 23: Example Crack Through Cross Section

(a) Dye Injection Device (b) Coring Setup

Figure 24: Coring Details

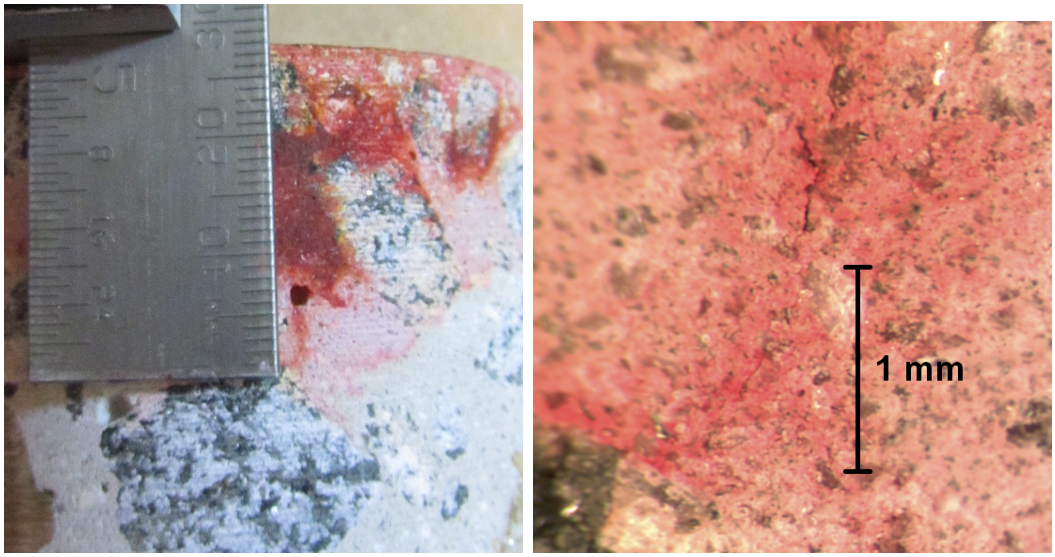

(a) Macroscopic View (b) Microscopic View of Crack Tip

Figure 25: Dyed Crack D

Finally, a sample dyed core is seen in figure 25. There is evidence that the dye also diffused through interconnected pores, but the crack is still distinguishable from the diffused dye as a darker line.

CHAPTER IV

RESULTS AND DISCUSSION

4.1 Results

4.1.1 #6 Bar Beam

The first beam tested contains two #6 bars. This beam is chosen because it is supposed to yield the deepest cracks. First, baseline measurements are taken to determine diffusivity, dissipation, longitudinal wave speed, and Rayleigh wave speed. Next the finite element simulation is run using the diffusion parameters listed in table 5 to obtain the relationship between crack depth and arrival time of maximum energy (ATME) seen in figure 26.

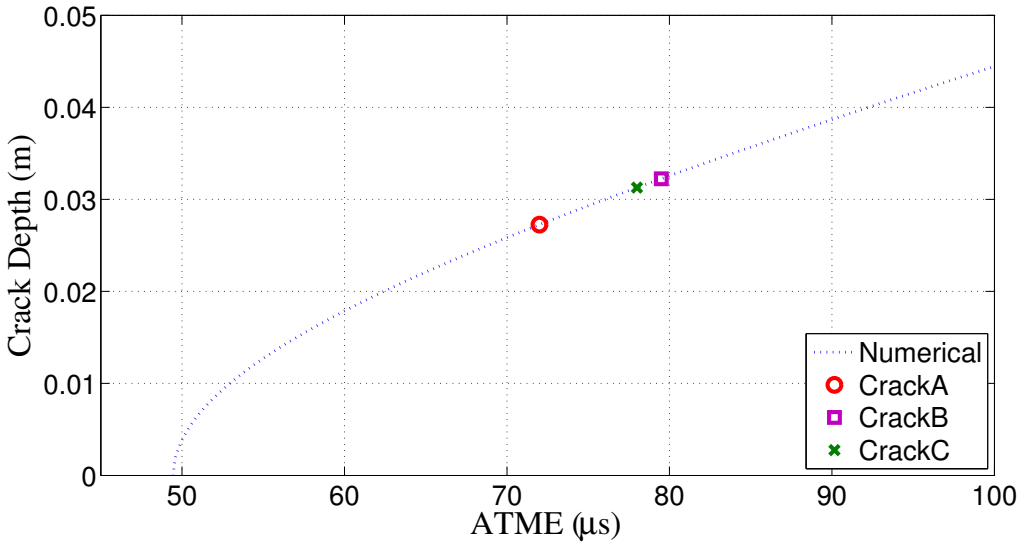

Figure 26: Depth as a Function of ATME for the Beam with #6 Bars

After baseline measurements were taken, the beam is cracked by taking it up to its maximum load. Once cracked, the beam is unloaded and both time of flight diffraction and diffusion measurements are taken. The energy evolution for the diffusion measurements, and their fitted curves, can be seen in figure 27.

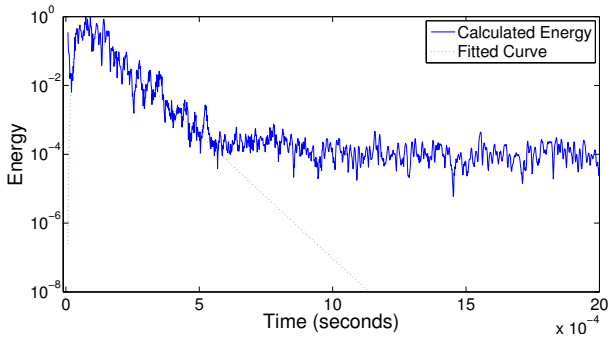

(a) Crack A

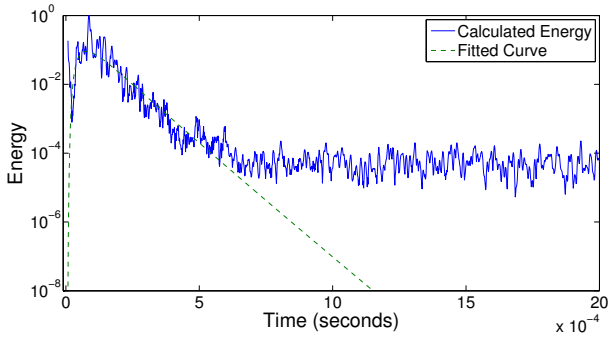

(b) Crack B

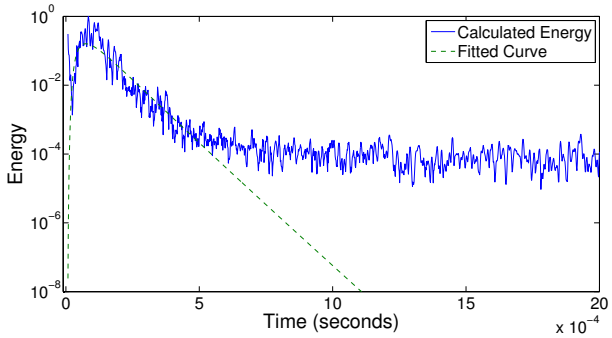

(c) Crack C

Figure 27: Energy Evolution for the Cracks on the Beam with #6 Bars

Finally, the results for the different measurement methods are plotted in figure 28. The diffusion results hovered around the same value, around 3cm, while the time of flight diffraction results hovered between 8cm and 10cm. The visual inspection method varied from 4cm to 8cm. All of these results fall short of the 16.5cm that was expected from this beam.

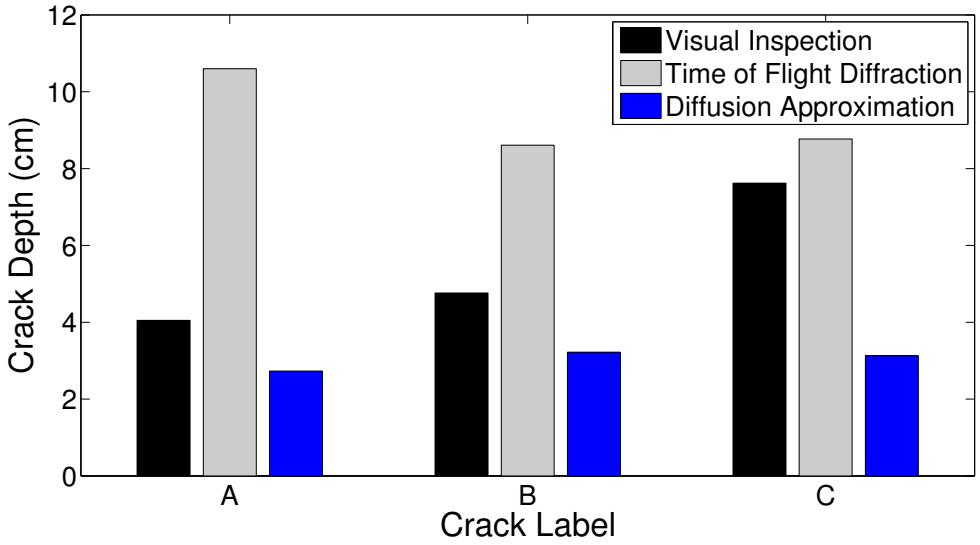

Figure 28: Comparison of the Estimation Methods on the Cracks on the Beam with #6 Bars

4.1.2 #8 Bar Beam

The second beam tested has two #8 bars. It is treated the same way as the first beam, but the cracks on this beam are chosen for validation via dye-injected cores. The relationship between crack depth and ATME can be seen in figure 29.

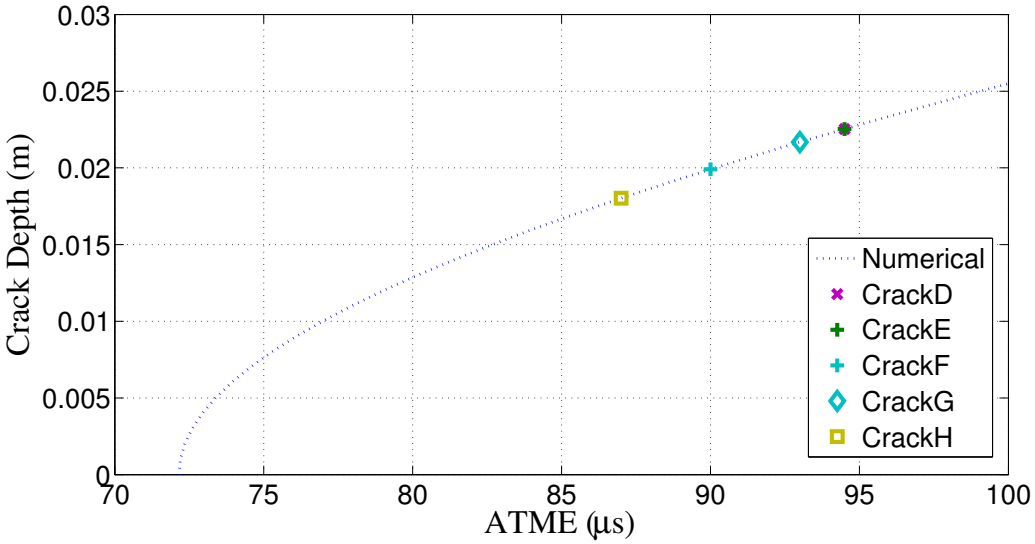

Figure 29: Depth as a Function of ATME for the Beam with #8 Bars

Unfortunately, this beam did not have enough space to do time of flight diffraction testing on every crack. All of the cracks were tested using the diffusion method and visual inspection, but cracks D and H were also interrogated using time of flight diffraction and coring. The energy evolution for each of the cracks can be seen in figure 30.

Finally, the results for the different measurement techniques were plotted in figure 31. Although the cracks were shallower than those found on the beam with the #6 beam, as expected, they still fell short of the 14.5cm expected. The time of flight diffraction method severely overestimated the actual crack depth while the other methods were closer.

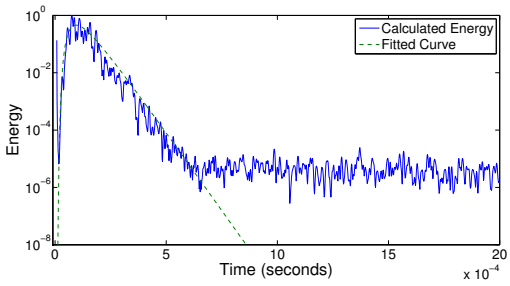

(a) Crack D

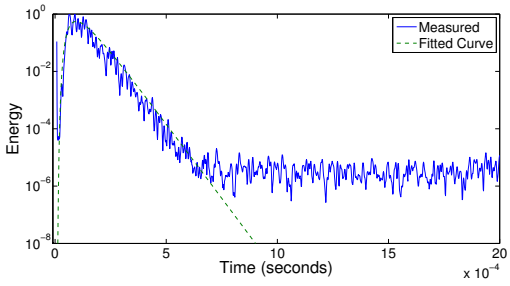

(b) Crack E

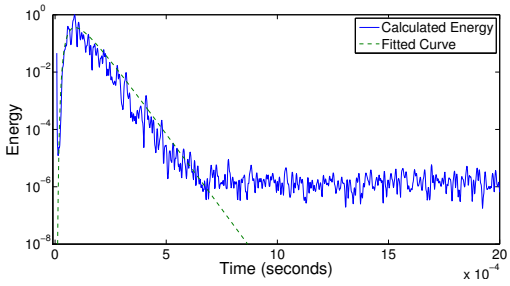

(c) Crack F

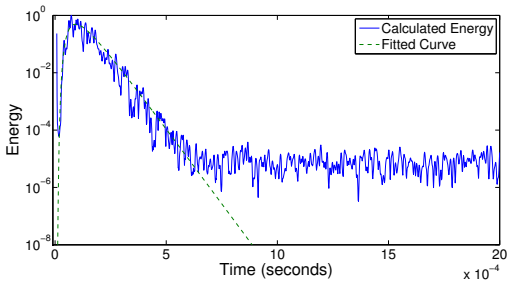

(d) Crack G

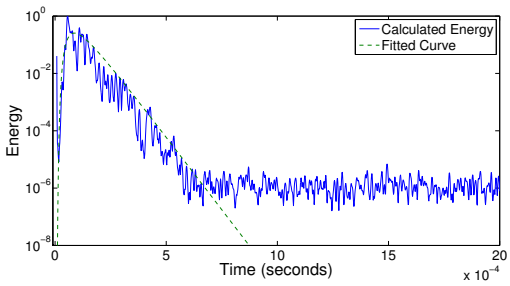

(e) Crack H

Figure 30: Energy Evolution for the Cracks on the Beam with #8 Bars

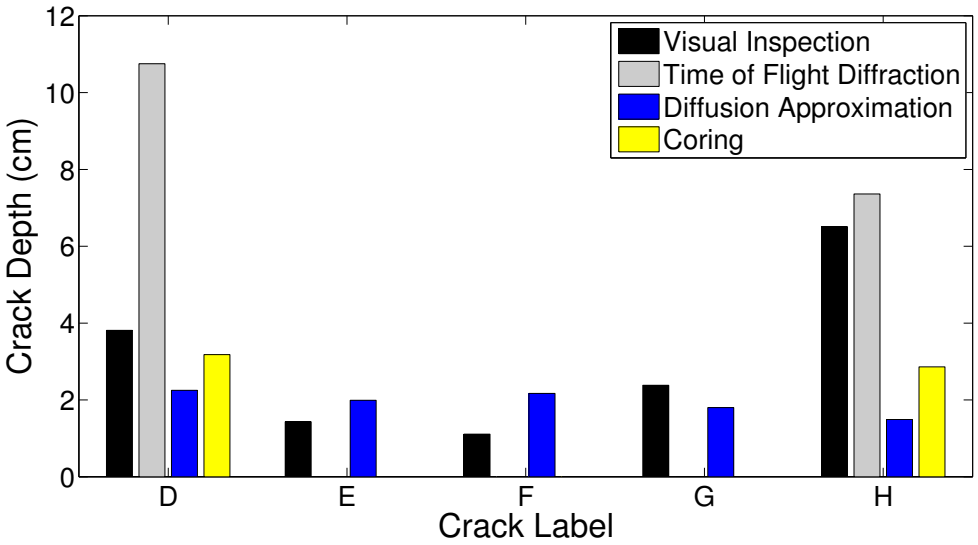

Figure 31: Comparison of the Estimation Methods on the Cracks on the Beam with #8 Bars

4.1.3 #7 Bar Beam

The third and final beam tested contains two #7 bars. The relationship between crack depth and ATME can be seen in figure 32.

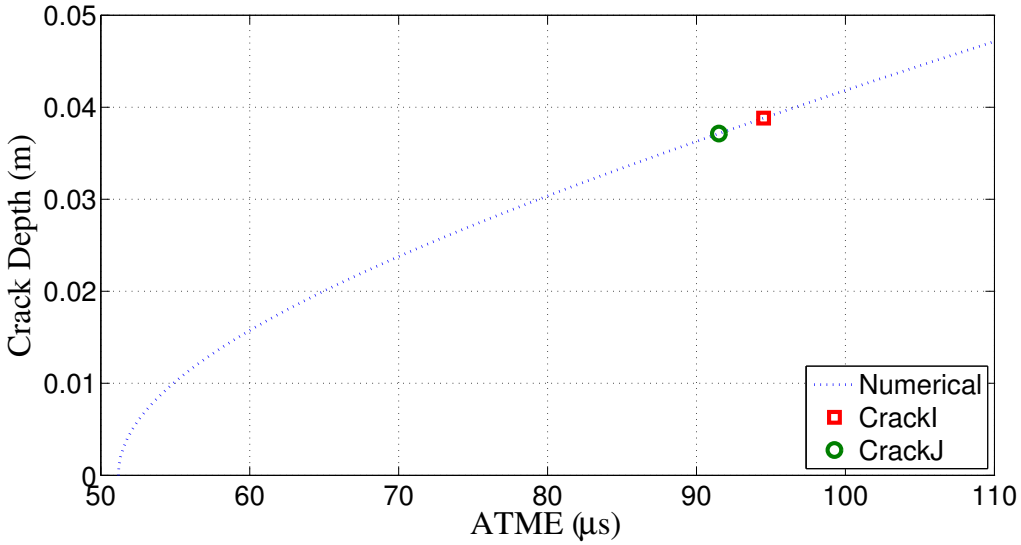

Figure 32: Depth as a Function of ATME for the Beam with #7 Bars

Both cracks on this beam were interrogated using the diffusion method and visual inspection. Crack I was further investigated using the time of flight diffraction technique.

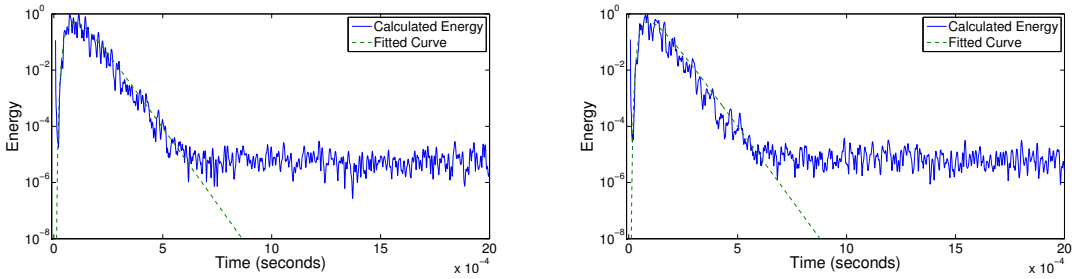

(a) Crack I (b) Crack J

Figure 33: Energy Evolution for the Cracks on the Beam with #7 Bars

Finally, the results for the different measurement techniques were plotted in figure 34. As suspected, the estimations were between those in the beams with #6 bars and #8 bars, but again, the depths fell short of the expected 15.5cm.

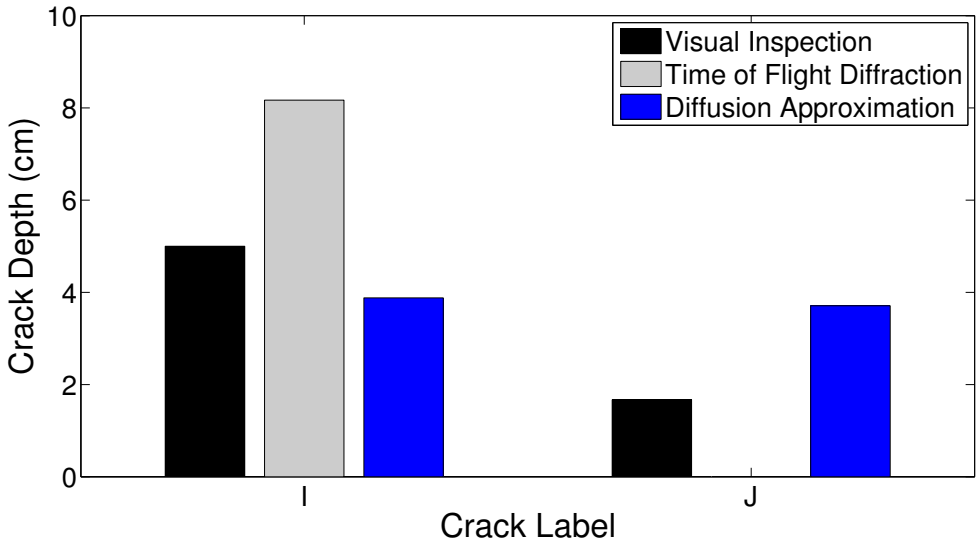

Figure 34: Comparison of the Estimation Methods on the Cracks on the Beam with #7 Bars

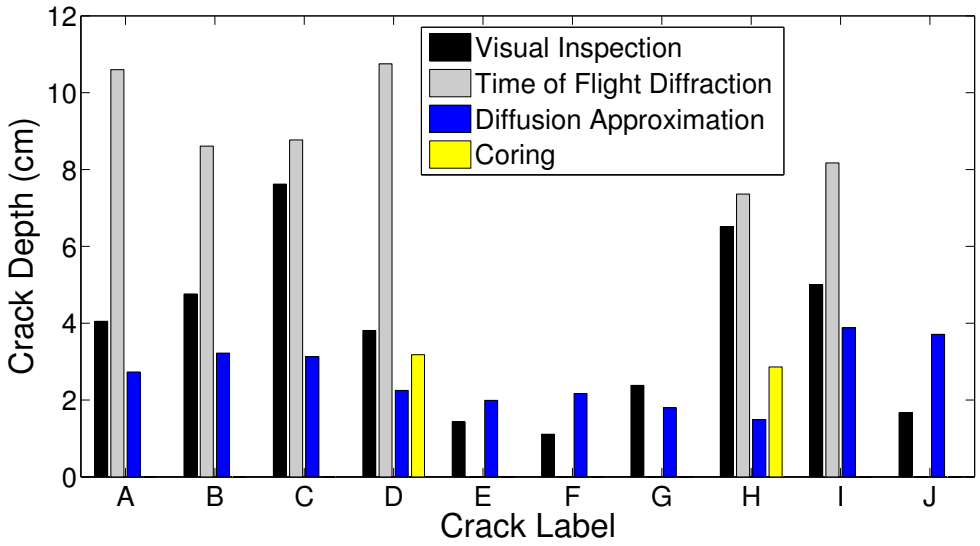

Figure 35: Comparison of the Estimation Methods on All of the Cracks

4.1.4 Summary

A comparison of the estimation methods on all of the cracks are plotted in figure 35. The time of flight diffraction method predicted a crack at least twice as deep as that predicted by the diffusion approximation for every case where both were used.

The visual inspection method predicted a large range of possible crack depths for cracks that should theoretically be the same (each beam should have cracks of roughly the same depth), which suggests that it is an unreliable method of crack depth estimation.

In both cases where coring was used to validate the crack depths, the diffusion approximation estimates most closely corresponded to the coring estimations, suggesting that the diffusion approximation method is the most accurate method of those tested.

The numerical data for figure 35 is tabulated in table 6.

4.2 Discussion

The visual inspection technique overestimates the crack depth when compared to the core result. Crack initiation tends to happen at imperfections and free surfaces, so a

Table 6: Crack Depth Measurements by Technique

Crack Label	Visual Inspection (cm)	Time of Flight Diffraction (cm)	Diffusion Approximation (cm)	Coring (cm)
A	4.05	10.60	2.73	N/A
B	4.76	8.61	3.22	N/A
C	7.62	8.77	3.13	N/A
D	3.81	10.75	2.25	3.18
E	1.43	N/A	1.99	N/A
F	1.11	N/A	2.17	N/A
G	2.38	N/A	1.80	N/A
H	6.51	7.36	1.49	2.86
I	5.00	8.17	3.88	N/A
J	1.67	N/A	3.71	N/A

deeper crack at the surface of the beam is to be expected. The time of flight diffraction technique also overestimates the crack depth when compared to the core result. Since the time of flight diffraction technique relies on an assumed path and assumed wave, but provides no method for validating that either is accurate, this overestimation is most likely due to a different path or wave than is assumed. Additionally, the impactor generates relatively low frequency waves, which have long wavelengths, meaning that the crack may be too small for such a low frequency regime to detect. Finally, the diffusion method most closely estimates the crack depth according to the core result.

Due to the larger space requirements necessitated by the time of flight diffraction technique, cracks that are spaced close together will not be measurable. Unfortunately, in especially damaged areas of concrete, i.e., ones that need assessing, the damage does not usually manifest itself as a single large crack, but rather several small cracks. This makes the time of flight diffraction technique difficult to apply in reality.

It is important to note that the core results do not directly measure how deep the crack is, but instead measure how deep the dye was able to impregnate the concrete using the previously described injection technique. The crack is not likely to be shallower than the core result suggests, but it may be deeper.

CHAPTER V

CONCLUSION AND FUTURE WORK

5.1 Conclusion

In this research, reinforced concrete beams were designed based on cross sectional analysis to yield a variety of crack depths for ultrasonic inspection. These beams were cast with different reinforcement: two #6 bars, two #7 bars, and two #8 bars. Each of these beams was loaded in four point bending until cracks developed. After the beams were unloaded, each crack was interrogated using the diffusion method and suitable cracks were interrogated using the time of flight diffraction technique. Finally, one of the beams had its suitable cracks injected with an acetone based dye followed by coring to validate the estimated crack depths.

The results suggest that the diffusion method is by far the most accurate method of those investigated in this research. On both of the cracks that were cored, the diffusion method was within 1.4cm of the cored crack depth. However, the diffusion approximation underestimated both crack D and crack H, suggesting that the diffusion approximation may require a safety factor to be used safely in the field. The time of flight diffraction method, on the other hand, consistently overestimated the true crack depth, which makes it the most conservative estimate. In this case, a conservative estimate is one that maximizes safety, while also costing the most in terms of repair.

5.2 Future Work

The time of flight diffraction technique was unreliable for the crack depths interrogated in this research, so future work would need to be done to validate the time of

flight diffraction technique for a variety of crack depths. Although not investigated in this research, the effect of the α angle will need further investigation. In this research, cracks had estimated depths allowing for a predetermined α angle, but in the field this may not be the case. A method for assessing the appropriate spacing of transducers will also need to be investigated before it can be effectively applied in the field to cracks of unknown depth.

The diffusion technique needs further testing to determine the error inherent in its estimations before being put to use in the field. Since the diffusion method relies on the cross sectional dimensions of the beam, further samples of varying cross sections should be tested. Additionally, diffusivity has a dependence on loading or state of stress, which made measurements under loading problematic. Diffusivity's dependence on state of stress would need to be investigated before the diffusion technique could be applied to most beams in situ, especially prestressed and post-tensioned beams. Diffusivity should also be investigated as a method of determining the state of stress in concrete.

The coring method used in this research would also need further investigation to confirm whether the depth of the dye penetration was the true depth of the crack.

REFERENCES

[1] Achenbach, J. D., *Wave propagation in elastic solids*. North-Holland Pub. Co, 1973.

[2] Achenbach, J., Komsky, I., Lee, Y., and Angel, Y., "Self–calibrating ultrasonic technique for crack depth measurement," *Journal of Nondestructive Evaluation*, vol. 11, pp. 103–108, Aug. 1992.

[3] Angel, Y. and Achenbach, J., "Reflection and transmission of obliquely incident rayleigh waves by a surface–breaking crack," *Journal of the Acoustical Society of America*, vol. 75, pp. 313–319, Feb. 1984.

[4] ANSYS, *ANSYS 13.0 Documentation*. ANSYS Inc., 2010.

[5] Anugonda, P., Wiehn, J. S., and Turner, J. A., "Diffusion of ultrasound in concrete," *Ultrasonics*, vol. 39, pp. 429–435, Aug. 2001.

[6] Becker, J., Jacobs, L. J., and Qu, J., "Characterization of cement-based materials using diffuse ultrasound," *Journal of Enineering Mechanics*, vol. 129, pp. 1478–1484, Dec. 2003.

[7] Carino, N. and Sansalone, M., "Pulse–echo medho for flaw detection in concrete," Tech. Rep. 1199, National Bureau of Standards, Washington, DC, July 1984.

[8] Carino, N., Woodward, K., Leyendecker, E., and Fattal, S., "A review of the skyline plaza collapse," *Concrete International*, vol. 5, pp. 35–42, July 1983.

[9] Cook, R., Malkus, D., Plesha, M., and Witt, R., *Concepts and applications of finite element analysis*. John Wiley & Sons. Inc, 2001.

[10] Deroo, F., Kim, J.-Y., Qu, J., Sabra, K., and Jacobs, L. J., "Detection of damage in concrete using diffuse ultrasound," *Journal of the Acoustical Society of America*, vol. 127, pp. 3315–3318, June 2010.

[11] Kee, S.-H. and Zhu, J., "Using air–coupled sensors to determine the depth of a surface–breaking crack in concrete," *Journal of the Acoustical Society of America*, vol. 127, pp. 1279–1287, Mar. 2010.

[12] Lin, Y., Liou, T., and Tsai, W.-H., "Determining crack depth and measurement errors using time-of-flight diffraction techniques," *ACI Materials Journal*, vol. 96, pp. 190–195, Mar. 1999.

[13] Lin, Y. and Su, W.-C., "Use of stress waves for determining the depth of surface-opening cracks in concrete structures," *ACI Materials Journal*, vol. 93, pp. 494–504, Sept. 1996.

[14] Popovics, J., Song, W.-J., Ghandehari, M., Subramaniam, K., Achenbach, J., and Shah, S., "Application of surface wave transmission measurements for crack depth determination in concrete," *ACI Materials Journal*, vol. 97, pp. 127–135, Mar. 2000.

[15] Powers, D. L., *Boundary Value Problems and Partial Differential Equations*. Academic Press, 2010.

[16] Ramamoorthy, S. K., Kane, Y., and Turner, J. A., "Ultrasound diffusion for crack depth determination in concrete," *Journal of the Acoustical Society of America*, vol. 115, pp. 523–529, Feb. 2004.

[17] Sansalone, M. and Carino, N., "Impact-echo method," *Concrete International: Design Construction*, vol. 10, no. 4, pp. 38–46, 1988.

[18] Sansalone, M., Lin, J.-M., and Streett, W. B., "Determining the depth of surface-opening cracks using impact-generated stress waves and time-of-flight techniques," *ACI Materials Journal*, vol. 95, pp. 168–177, Mar. 1998.

[19] Seher, M., In, C.-W., Kim, J.-Y., Kurtis, K. E., and Jacobs, L. J., "Numerical and experimental study of crack depth measurement in concrete using diffuse ultrasound," *Journal of Nondestructive Evaluation*, vol. 32, pp. 81–92, Mar. 2013.

[20] Sheng, P., *Introduction to Wave Scattering, Localization and Mesoscopic Phenomena*. Springer, 2006.

[21] Song, W.-J., Popovics, J., Aldrin, J., and Shah, S., "Measurement of surface wave transmission coefficients across surface-breaking cracks and notches in concrete," *Journal of the Acoustical Society of America*, vol. 113, pp. 717–725, Feb. 2003.

[22] Survey, U. G., "Mineral commodity summaries," tech. rep., U.S. Department of the Interior, Feb. 2014.

[23] Weaver, R. L. and Sachse, W., "Diffusion of ultrasound in a glass bead slurry," *Journal of the Acoustical Society of America*, vol. 97, pp. 2094–2102, Apr. 1995.

[24] Wu, T.-T., Fang, J.-S., and Liu, P.-L., "Detection of the depth of a surface-breaking crack using transient elastic waves," *Journal of the Acoustical Society of America*, vol. 97, pp. 1678–1686, Mar. 1995.

[25] Zhao, Y., Ren, H., Dai, H., and Jin, W., "Composition and expansion coefficient of rust based on x-ray diffraction and thermal analysis," *Corrosion Science*, vol. 53, pp. 1646–1658, June 2011.